Journal of
Applied
Crystallography
ISSN 0021-8898

Received 14 August 2006
Accepted 17 January 2007

Two-dimensional small-angle X-ray scattering from as-grown and heat-treated synthetic quartz

Pedro L. Guzzo,[a]* Armando H. Shinohara,[b] Anastacia E. F. Santos,[b] Sérgio S. Funari[c] and Shigeo Daito[d]

[a]Department of Mining Engineering, Federal University of Pernambuco, Brazil, [b]Department of Mechanical Engineering, Federal University of Pernambuco, Brazil, [c]Hamburg Synchrotron Radiation Laboratory, Germany, and [d]Schlumberger–Doll Research Center, USA. Correspondence e-mail: pguzzo@ufpe.br

The small-angle X-ray scattering (SAXS) in as-grown and heat-treated quartz crystals was investigated as a function of the azimuth angle around the primary beam. For this, samples parallel to $(10\bar{1}0)$ were extracted from Z- and −X-growth sectors of a synthetic quartz bar which had the OH content evaluated by infrared spectroscopy (IRS). In addition, SAXS and IRS were independently recorded as a function of heating temperature. As a result, the two-dimensional SAXS images revealed an anisotropic pattern randomly decorated by low-intensity Kossel lines. The intensities were projected along specific directions or were axially integrated around the primary beam. It was observed that the Porod invariant (Q) increased and the Kossel lines moved slightly to higher q values with increasing temperature. The effect of the sample orientation on the Q value and the lack of a clear relationship between Q and OH content suggested that the diffuse scattering due to the periodicity of the crystal lattice played an important role in the small-angle scattering of quartz. The net scattering intensities produced by heat-treatment at 873 K were attributed to molecular water aggregates created by the diffusion of as-grown OH defects.

1. Introduction

Synthetic quartz is widely used in piezoelectric resonators as frequency and time standards, filters, transducers and sensors. Renewed interest in the quality and uniformity of as-grown crystals emerged with the demand of small resonators for high-frequency devices and high-performance sensors used in severe environments with temperature, pressure and vibration loadings (Balascio & Lind, 1997; Eernisse, 2001). Synthetic quartz is produced by hydrothermal dissolution of natural quartz *lascas* in aqueous basic solvents under high temperature and high pressure. Consequently, water-related defects are inevitably present during crystal growth (Aines *et al.*, 1984; Cordier & Doukhan, 1991). In addition, it is well known that certain quartz becomes milky after prolonged heat treatments at temperatures higher than 773 K due to the coalescence of water precipitates (Dood & Fraser, 1967; Bambauer *et al.*, 1969; Suzuki *et al.*, 1980). The diffusion mechanism under which as-grown OH defects give rise to molecular water aggregates remains unclear and little is known about this mechanism when commercial synthetic quartzes, which are grown today with OH content as low as a few tens of p.p.m. (parts per million), are currently annealed in mild temperatures during the fabrication process of quartz resonators (Boy *et al.*, 1993).

In previous work, the clustering of water aggregates was investigated in samples from typical growth sectors of a Z-plate synthetic quartz, coupling small-angle X-ray scattering (SAXS) and infrared spectroscopy (IRS) (Guzzo *et al.*, 2003). As a result, no clear relationship was observed between the OH content and the radius of water aggregates calculated from the scattering curves. In addition, small-angle scattering was unexpectedly observed in as-grown specimens with low OH content. This surprising result was tentatively explained by assuming the presence of tiny water aggregates dispersed in the quartz matrix, as observed by McLaren *et al.* (1983) and Cordier & Doukhan (1991) using transmission electron microscopy (TEM) of synthetic quartz with very high OH content. Furthermore, discontinuities noticed in the scattering intensity curves were not entirely clarified and remained open for further investigations.

Recently, the availability of two-dimensional detectors coupled with synchrotron radiation sources led to the investigation of anisotropic small-angle scattering in condensed matter systems. For instance, two-dimensional SAXS was used to characterize the distribution of bulk grown-in micro-defects in germanium wafers (Poelman *et al.*, 2004). Until now, scattering at small-angles has not been investigated for the study of anisotropy of the quartz crystal lattice. Thus, the aim of the present work was to advance the analysis of the small-angle scattering of as-grown and heat-treated synthetic quartz as a function of the azimuth angle around the primary beam. For this, the SAXS patterns of specimens parallel to $(10\bar{1}0)$ and SC-cut planes were recorded before and after heating the samples at 473 K and 873 K. Real-time IRS and SAXS were independently carried out up to 473 K and 523 K, respectively. After subtracting the scattering measured in the as-grown condition, the scattering produced by the heat treatment was associated with the formation of molecular water aggregates.

2. Experimental procedure

Commercial synthetic quartz plates parallel to the SC-cut had their thickness reduced by successive lapping steps with coarse and fine

SiC grits. In the final stage of lapping, grits with a mean grain size of 2 μm were used. The SC-cut is an ordinary orientation of quartz used in the resonator industry. It is obtained by rotating the $(10\bar{1}0)$ plane by 22° around [0001], followed by a rotation of 34° with respect to $[11\bar{2}0]$. Throughout this study, the SC-cut specimens will be referred as double-rotated samples. In addition, un-rotated $(10\bar{1}0)$ samples were extracted from Z- and −X-growth sectors of a Z-plate synthetic quartz. The specimens for SAXS were prepared with thickness < 180 μm, giving $\mu t = 1.6$, where μ is the linear absorption coefficient and t is the thickness. The specimens for IRS were optically polished after reaching a thickness of 1.5 mm. IR spectra were obtained at different temperatures from 298 K up to 473 K with an unpolarized beam using an FTLA2000 ABB Bomen spectrometer. The samples were positioned between two metallic windows with diameter of 3 mm and heated at 2 K min^{-1} using a 3000 TM Specac temperature cell controller. Each spectrum was recorded after 100 scans from 7500 to 500 cm^{-1} with a resolution better than 4 cm^{-1}.

SAXS measurements were carried out at the Soft Condensed Matter A2 beamline at HASYLAB using an X-ray wavelength of 0.15 nm. The scattered X-rays were collected in a vacuum using a two-dimensional solid-state charge-coupled MARCCD 165 detector with an effective area of 210 cm^2. High-resolution images with 2048 × 2048 pixels were obtained. The sample–detector distance was fixed at 3100 mm. The spatial calibration of the SAXS camera was carried out using collagen, mineralized rat tail tendon standard. The SAXS patterns were collected at room temperature for as-grown and heat-treated samples. The heat treatments were carried out in a muffle furnace at atmospheric pressure at 473 K for 20, 40 and 60 h and at 873 K for 20 h. The heating rate was set at 1 K min^{-1}. Two-dimensional patterns were also recorded as a function of temperature from 298 K to 523 K. The samples were heated at a rate of 5 K min^{-1} in an electric furnace (Gehrke, 1989) and kept at fixed temperatures for 10 min prior to recording the SAXS patterns.

The data analyses of the SAXS patterns were performed using the *FIT2D* software (Hammersley, 1997). One-dimensional profiles were obtained by integrating the scattering intensities over an angular sector of 180° around the direction of the primary beam. One-dimensional profiles were also obtained by projecting a rectangular slice 50 pixels thick onto specific directions within the SAXS pattern. All curves were scaled to the incident beam and corrected for sample absorption and parasitic scattering. The angular range of the scattering curves was $0.10\ nm^{-1} \leq q \leq 1.05\ nm^{-1}$, where q is the magnitude of the scattering vector, defined as $4\pi\sin\theta/\lambda$, where 2θ is the scattering angle and λ is the wavelength of the primary beam.

3. Results and discussion

3.1. Two-dimensional scattering patterns

Fig. 1 shows typical two-dimensional SAXS patterns obtained from as-grown samples with $(10\bar{1}0)$ and double-rotated orientations. Essentially, the two-dimensional images consist of a central anisotropic pattern and streak lines either crossing the centre or not. The presence and position of the streak lines are sensitive to the position of the sample in the holder. Whereas the central pattern rotates with the same angle when the sample is turned around the primary beam without much other change, the position and intensity of the streak lines change randomly. Compared to the central pattern, the streak lines had very low intensity, which became quite strong when they crossed the beam centre, *i.e.* the zero node of the reciprocal lattice. Based on these observations, it is suggested that the scattering process which gives rise to these lines is the same as that for Kossel lines (Kossel *et al.*, 1935; Ullrich *et al.*, 1994; Nishikawa *et al.*, 2001). When a single crystal is positioned normal to the beam of collimated synchrotron rays, the atoms of the crystal lattice themselves become independent sources of monochromatic radiation. The waves emanating from any point within the lattice are reflected at the lattice planes at angles that correspond to Bragg's law, giving rise to diffraction lines on the X-ray detector.

Fig. 1(*a*) was obtained with the sample positioned with its [0001] direction parallel to the horizontal alignment of the detector. The central pattern shows a twofold symmetry with 1:1.05 aspect ratio between $\mathbf{H}_{0001}$ and $\mathbf{H}_{11\bar{2}0}$, where **H** represents a vector in reciprocal space. In a previous study, it was observed that the SAXS pattern showed a sixfold symmetry when samples parallel to (0001) were positioned perpendicular to the primary beam (Guzzo *et al.*, 2003*b*). In quartz, the axis perpendicular to $(10\bar{1}0)$ and (0001) has onefold and threefold symmetry, respectively. The higher symmetry noticed in the SAXS patterns comes from the fact that scattering of X-rays by a set of lattice planes is a centrosymmetric property. Thus, the two-dimensional pattern recorded around the direct beam reveals the symmetry corresponding to the specimen orientation and may be

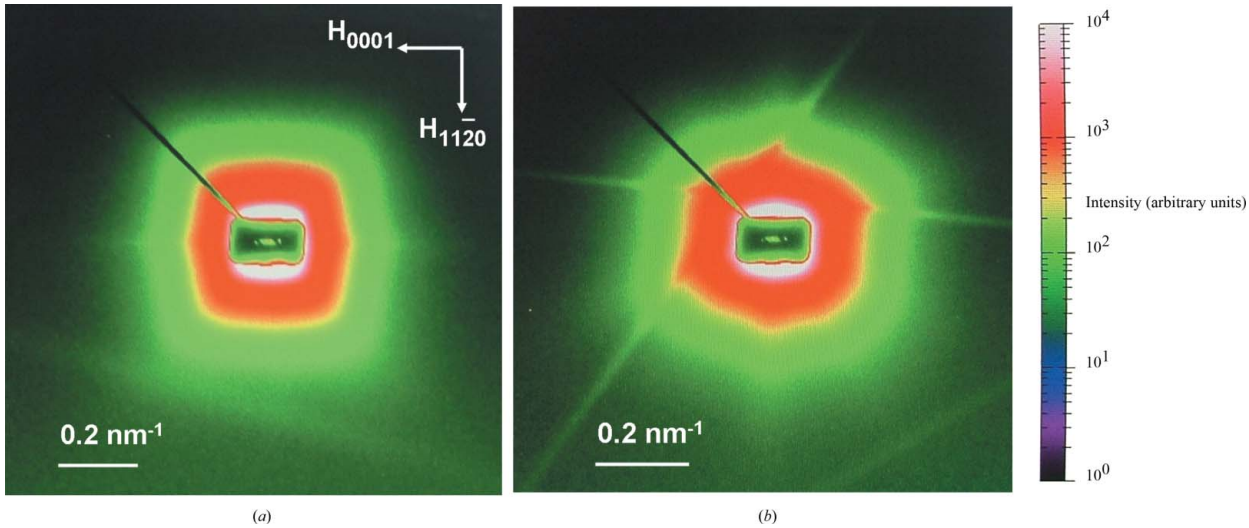

Figure 1
Two-dimensional SAXS patterns of as-grown samples of synthetic quartz. (*a*) Un-rotated $(10\bar{1}0)$. (*b*) Double-rotated $(10\bar{1}0)$.

attributed to the three-dimensional periodicity of the crystal structure or to the three-dimensional periodicity of phonons due to thermal diffusion scattering (Vainshtein, 1996). The scattering around the zero node of the reciprocal lattice may be similar to the scattering found near the tails of a Bragg peak, known as Huang diffuse scattering (Grasse *et al.*, 1981; Vainshtein, 1996).

The scattering patterns shown in Fig. 1 may also have a contribution from a mosaic structure formed by many small blocks of slightly differently oriented material in the apparently strictly single crystal. The distorted twofold symmetry noticed in Fig. 1(*b*) suggests an additional misalignment of the crystal structure along a crystallographic plane because the SC-cut is not parallel to a natural crystal plane. Further attempts are required to clarify the contribution of diffuse scattering and mosaic structure in the small-angle scattering of near perfect crystals such as quartz.

3.2. Effect of the heat treatment

The angular dependence of the anisotropic scattering was initially analysed using $(10\bar{1}0)$ samples extracted from Z- and −X-growth sectors. Fig. 2 shows typical one-dimensional profiles obtained by projecting the scattering intensities along $\mathbf{H}_{0001}$, $\mathbf{H}_{11\bar{2}1}$ and $\mathbf{H}_{11\bar{2}0}$, corresponding to directions perpendicular to (0001), $(11\bar{2}1)$ and $(11\bar{2}0)$ planes, respectively. For as-grown samples, Fig. 2(*a*) shows that the scattering intensities decrease exponentially with increasing q. It is observed that the projected intensities along $\mathbf{H}_{11\bar{2}1}$ are slightly higher than those found for $\mathbf{H}_{11\bar{2}0}$ and $\mathbf{H}_{0001}$. In Fig. 2(*a*), the increase in the SAXS intensity recorded at $q = 0.4$ nm^{-1} in the $\mathbf{H}_{11\bar{2}0}$ direction is due to the overlap with a Kossel line. After heat treatment, the scattering intensities increased and the profiles deviated from exponential decay in the q range from 0.4 to 0.7 nm^{-1}. It is also noticed that the scattering along $\mathbf{H}_{11\bar{2}0}$ exceeds the intensity recorded along $\mathbf{H}_{11\bar{2}1}$.

In order to eliminate the effect of the diffuse scattering due to the crystal lattice, the scattering intensities of the as-grown samples were subtracted from the corresponding curves of heat-treated ones. This procedure was successfully adopted by Grasse *et al.* (1981) to evaluate the diffuse X-ray scattering from neutron-irradiated quartz crystals. Fig. 3 shows that the net effect of the heat treatment is better observed along $\mathbf{H}_{11\bar{2}0}$ for the sample from the −X-growth sector. The effect of the heat treatment is considerably lower for the specimen from the Z-growth sector. Thus, the increase in the scattering intensity produced by the heat treatment occurs essentially in the −X-growth sector along the $[11\bar{2}0]$ direction.

The effect of the heat treatment on the SAXS patterns was also analysed by integrating the scattering intensities within a sector of 180° around the primary beam. This procedure was applied for $(10\bar{1}0)$ and double-rotated samples in as-grown and heat-treated conditions. As a result, similar exponential decays as shown in Fig. 2(*a*) were obtained. In the case of double-rotated samples, the heat treatments performed at 473 K did not affect the shape of the one-dimensional curves. A clear effect of heat treatment was only noticed in $(10\bar{1}0)$

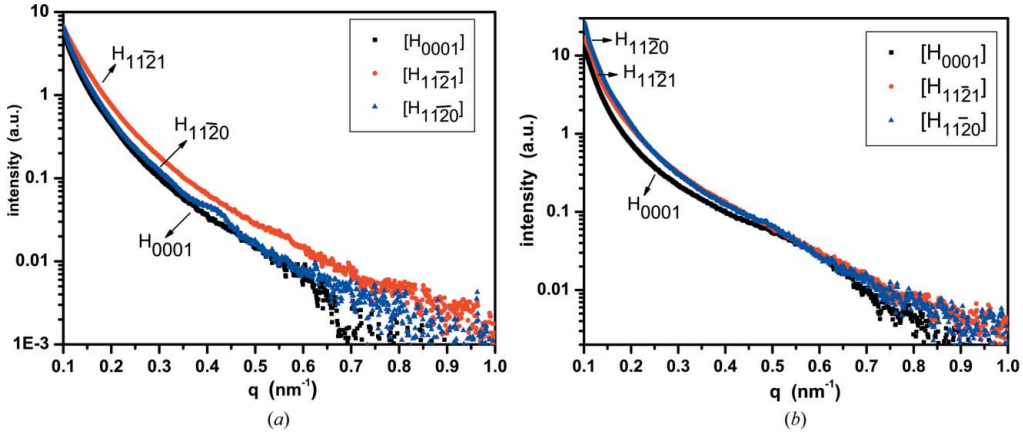

Figure 2
SAXS intensity in the $\mathbf{H}_{0001}$, $\mathbf{H}_{11\bar{2}1}$ and $\mathbf{H}_{11\bar{2}0}$ directions for −X-growth sector sample (*a*) before and (*b*) after heat treatment at 873 K in synthetic quartz.

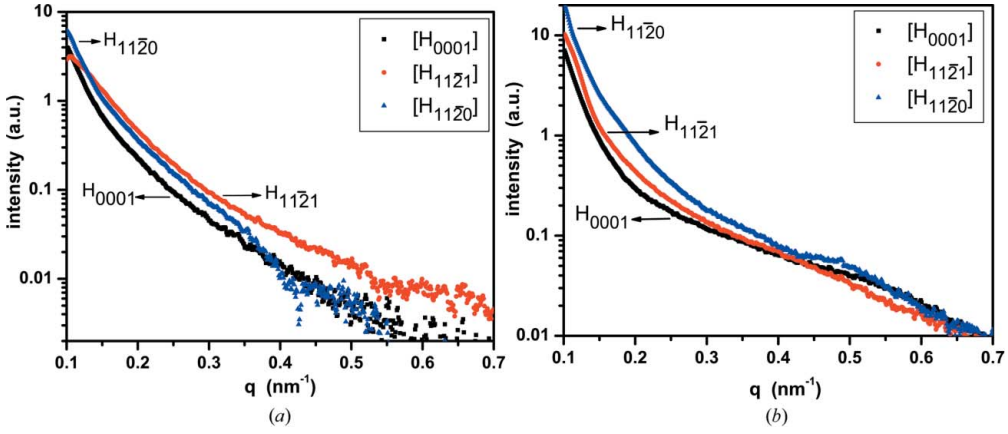

Figure 3
Net scattering intensity in the $\mathbf{H}_{0001}$, $\mathbf{H}_{11\bar{2}1}$ and $\mathbf{H}_{11\bar{2}0}$ directions due to heat treatment at 873 K in synthetic quartz. (*a*) Z-growth sector. (*b*) −X-growth sector.

Table 1
Porod's invariant (Q) and OH content for as-grown and heat-treated samples.

Sample	Q	OH (N/10^6Si)	Q	OH (N/10^6Si)
(1010)*	As-grown		Heat treated at 473 K	
20 h	0.0112	15	0.0090	–
40 h	0.0106	16	0.0106	–
60 h	0.0112	15	0.0111	–
(1010)	As-grown		Heat treated at 873 K	
Z-sector	0.0065	40	0.0116	48
Z-sector	0.0055	40	0.0098	48
−X-sector	0.0089	362	0.0191	416

* Double rotated. – Not measured.

samples heat-treated at 873 K. These curves were used to determine the Porod invariant (Q) calculated numerically according to the procedure described by Patel & Schmidt (1971). As defined elsewhere, Q, which is equal to the mean square value of the excess scattering density, is independent of the structure of the scattering centres, being dependent on the volume fraction and the electron density contrast of these centres (Koch *et al.*, 2003). Table 1 summarizes the Q values calculated from as-grown and heat-treated samples. In the as-grown condition, the Q values for $(10\bar{1}0)$ samples are lower than those found by double-rotated samples, indicating the effect of the crystal orientation on the scattering intensity. It is also noticed that double-rotated samples submitted to mild heat treatment did not show substantial differences in Q values.

Fig. 4 shows the IR spectra obtained from Z- and −X-growth sectors prior to and after the heat treatment at 873 K. Basically, these spectra are composed of a sharp band at 3585 cm^{-1}, assigned to the so-called as-grown OH point defect (Lipson & Kahan, 1985), superposed upon a broad band due to fundamental O–H stretching from Si–OH and H_2O compounds (Aines *et al.*, 1984). As was originally assigned by Kats (1962), the bands at 3296 and 3194 cm^{-1} are due to quartz overtone or combination bands of the Si–O lattice.

The OH content shown in Table 1 was evaluated by numerical integration using the calibration proposed by Paterson (1982). For the −X-growth sector, it is clearly observed that the heat treatment at 873 K decreased the intensity of the sharp band at 3585 cm^{-1} and increased the width of the broad band. This result can be attributed to an increase in the concentration of molecular water defects due to the coalescence of as-grown OH point defects. Previously, it was reported that the incorporation of OH-related defects was responsible for the growth striations appearing in X-ray diffraction topographies of the −X-growth sector (Iwasaki, 1980; Iwaski *et al.*, 1990). Thus, the scattering intensities recorded along $\mathbf{H}_{11\bar{2}0}$ suggest that the linear density of water aggregates is higher along the $[11\bar{2}0]$ direction. After heat treatment at 873 K, the increase in the Q value is related to the formation of water aggregates and this increase is remarkable for the −X-growth sector due to its high OH content in the as-grown condition.

Besides the broad band recorded in the region from 3600 to 3000 cm^{-1}, additional evidence for the formation of molecular water clusters was not found in the IR spectra. The absence of the absorption at 1630 cm^{-1} due to the fundamental bending mode of H_2O molecules and those absorptions at 5200 cm^{-1} due to the combination and overtones of the H_2O vibration modes can be explained by the low absorptivity of H_2O defects in quartz. These bands are observed only in IR spectra from samples that are several millimetres thick or have very high OH content (Aines *et al.*, 1984; Cordier & Doukhan, 1991).

3.3. Real-time measurements

In situ SAXS and IRS were independently carried out in double-rotated samples over the temperature range 298 K to 525 K. In order to quantify the SAXS intensity and the IR absorption changes as a function of temperature, the invariant Q and the absorbance (A) at 3400 cm^{-1} were determined. The absorbance values were normalized by the sample thickness. The relationships found using these procedures are summarized in Fig. 5. As a result, increasing the temperature broadened the OH band and decreased its integral absorbance. Similar behavior was noticed for the Si–O absorption bands. Upon cooling, the original features of the IR spectra were restored and no change in the broad OH band was detected when room temperature was reached. According to Beer–Lambert's law, absorbance is proportional to the water content and the sample thickness, by way of the molar absorption coefficient. Thus, the decrease noticed in the absorbance of the broad OH band is associated with the decrease in the molar absorptivity of the OH-related defects. The changes in the molar absorptivity of these defects at this range of temperature were interpreted to be due to changes in OH bond length influenced by the thermal expansion of the quartz structure (Suzuki & Nakashima, 1999).

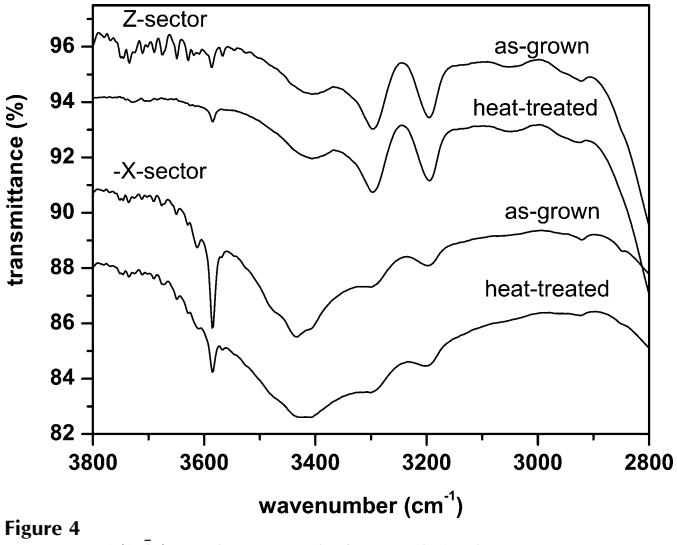

Figure 4
IR spectra of $(10\bar{1}0)$ samples measured prior to and after heat treatment at 873 K. The spectra are displaced from their original transmittance positions.

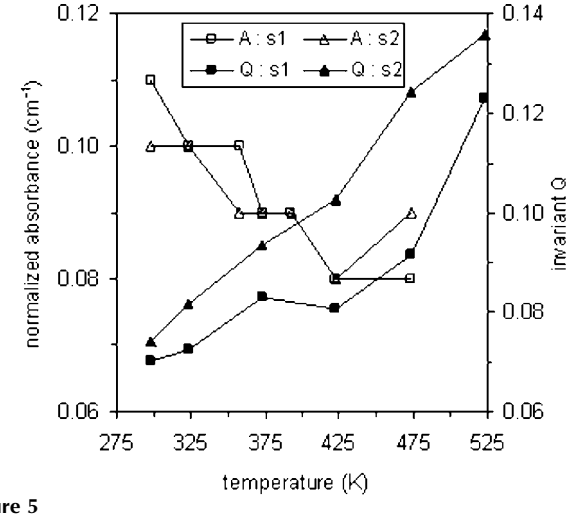

Figure 5
Effect of temperature on the Porod invariant (Q) and absorbance (A) during the heating cycle for two specimens (s1 and s2) with double-rotated $(10\bar{1}0)$ orientation.

The relationships found for Q and the absorbance at 3400 cm^{-1} shown in Fig. 5 are quite different when increasing the temperature. This observation supports the assumption that the main reason for the anisotropic scattering recorded in as-grown samples is connected to the diffuse scattering of the quartz lattice. As previously reported (Iwasaki, 1980; Suzuki *et al.*, 1980), the formation of molecular water aggregates takes place at temperatures much higher than that used in the *in situ* IR and SAXS measurements. In addition, the loss of OH species during this experiment is considered negligible due to the reversibility of the IR spectra. Thus, the increase in the Q value with increasing temperature shown in Fig. 5 suggests that thermal diffusion scattering also contributes to the whole diffusive scattering.

Besides the increase in the scattering intensity of the central pattern, changes in Kossel line properties were observed during the heating cycles. The profiles shown in Fig. 6 were obtained by projecting the scattering intensity onto a direction passing perpendicularly through a single line. As a result, it is observed that the Kossel line shifted towards high q values with increasing temperature. The inset plots shown in this figure show that the displacement of the Kossel line is linearly correlated with the temperature and its intensity changes during the heating. By tracking the peak position, referred to its maximum intensity, it is noticed that this line moved from 0.520 to 0.594 nm^{-1}. Upon cooling, this line moved back and its intensity decreased. In real space, these shifts are probably connected with atomic displacements from the lattice plane corresponding to the Bragg plane responsible for this line.

The results shown in Fig. 6 suggest that SAXS optics are suitable to obtain reliable fractions of the Kossel pattern from a thin single crystal as a function of external variables such as temperature. Similarly to the Kossel and X-ray rotation–tilt techniques (Bauch *et al.*, 2003), this method can be optimized to record changes in short-range periodicity of the crystal lattice, such as variation in lattice parameter and formation of structural defects induced by irradiation, together with the SAXS patterns using single experimental setting.

4. Concluding remarks

The results of this study can be summarized as follows.

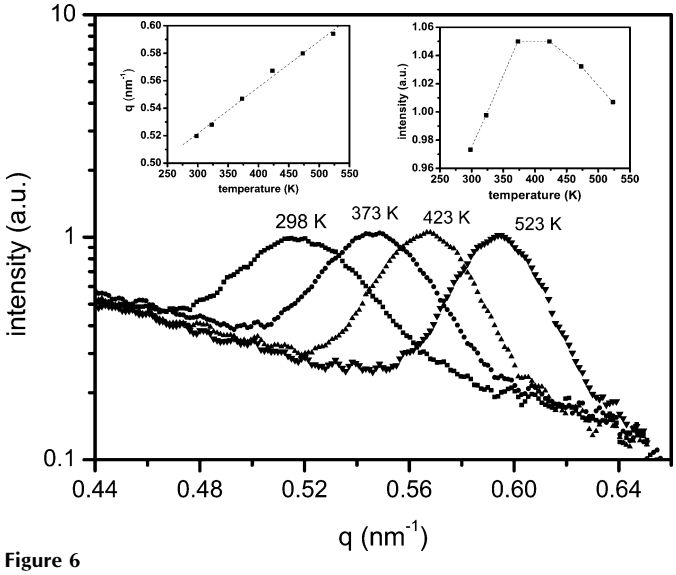

Figure 6
SAXS intensity measured at different temperatures, showing the shift in Kossel line position and intensity.

The small-angle scattering of synthetic quartz recorded with a two-dimensional detector was related to the symmetry of the crystal plane positioned perpendicular to the primary beam. The scattering intensities in as-grown samples obtained at room temperature were attributed to the diffuse scattering appearing around the origin of the reciprocal lattice. The streak lines randomly observed in the two-dimensional patterns were associated with Kossel lines.

Heat-treatments carried out at 873 K in $(10\bar{1}0)$ specimens modified the scattering intensities along the $[11\bar{2}0]$, $[11\bar{2}1]$ and [0001] directions in relation to the as-grown condition. In the low-q region, the net scattering was higher along $[11\bar{2}0]$ for the −X-growth sector, due to the formation of molecular water aggregates from OH-related point defects incorporated during the growth process. The heat treatments performed for up to 60 h at 473 K did not affect the scattering profiles of quartz samples extracted from the Z-growth sector.

The increase in the Porod invariant with heating temperature was attributed to thermal diffusion due to the expansion of the quartz lattice. Thus, thermal diffusion scattering should contribute to the intrinsic crystal diffuse scattering at room temperature. The position and intensity of the Kossel lines was also sensitive to increasing temperature, suggesting that SAXS can also be used to obtain reliable fractions of the Kossel pattern from rather perfect single crystals.

This work was supported by HASYLAB (project I-02-075), FVA/FINEP (Fundo Verde-Amarelo/Financiadora de Estudos e Projetos) and PROFIX/CNPq (Programa de Fixação de Doutores/Conselho Nacional de Desenvolvimento Científico e Tecnológico). PLG wishes to thank the Alexander von Humboldt Foundation for support for his stay in Hamburg, during which this study was initiated. He is also grateful to Dr M. H. J. Koch (EMBL, Hamburg) and Dr W. Bras (ESRF) for fruitful discussions. AEFS is grateful for a scholarship provided by CAPES (Coordenação de Aperfeiçoamento de Pessoal de Nível Superior).

References

Aines, R. D., Kirby, S. H. & Rossman, G. R. (1984). *Phys. Chem. Miner.* **11**, 204–212.
Aines, R. D. & Rossman G. R. (1984). *J. Geophys. Res.* **89**, 4059–4071.
Balascio, J. F. & Lind, T. (1997). *Curr. Opin. Solid State Mater. Sci.* **2**, 588–592.
Bambauer, H. U., Brunner, G. O. & Laves, F. (1969). *Am. Mineral.* **54**, 718–724.
Bauch, J., Ulrich, H. J., Böhling, M. & Reiche, D. (2003). *Cryst. Res. Technol.* **38**, 440–449.
Boy, J. J., Berthaut, A., Renard, G., Roy, R., Thiebaud, D., Robichon, G. & Longet, C. (1993). *Proceedings of the 7th European Frequency and Time Forum*, pp. 57–62.
Cordier, P. & Doukhan, J. C. (1991). *Am. Mineral.* **111**, 361–369.
Dood, D. M. & Fraser, D. B. (1967). *Am. Mineral.* **52**, 149–160.
EerNisse, E. P. (2001). *Jpn. J. Appl. Phys.* **40**, 3479–3483.
Gehrke, R. (1989). *Top. Curr. Chem.* **151**, 113–159.
Grasse, D., Kocar, O., Peisl, H., Moss, S. C. & Golding, B. (1981). *Phys. Rev. Lett.* **46**, 261–264.
Guzzo, P. L., Shinohara, A. H., Pasquali, M. A., Gusken, E., Suzuki, C. K., Azevedo, W. A. & Mikawa, Y. (2003). *J. Appl. Cryst.* **36**, 459–463.
Guzzo, P. L., Shinohara, A. H., Schwartz, M. & Funari, S. S. (2003*b*). *HASYLAB Ann. Rep.* pp. 215–216.
Hammersley, A. (1997). http://www.bio.aps.anl.gov/mirror/www.esrf.fr/FIT2D
Iwasaki, F. (1980). *Jpn. J. Appl. Phys.* **19**, 1247–1256.
Iwaski, F., Shinohara, A. H., Iwasaki, H. & Suzuki, C. K. (1990). *Jpn. J. Appl. Phys.* **29**, 1139–1142.
Kats, A. (1962). *Philips Res. Rep.* **17**, 113–195, 201–279.
Koch, M. H. J., Vachette, P. & Svergun, D. I. (2003). *Q. Rev. Biophys.* **36**, 147–227.
Kossel, W., Loeck, V. & Voges, H. (1935). *Z. Phys.* **94**, 139–142.
Lipson, H. G. & Kahan, A. (1985). *J. Appl. Phys.* **58**, 963–970.
McLaren, A. C., Cook, R. F., Hyde, S. T. & Tobin, R. C. (1983). *Phys. Chem. Miner.* **9**, 79–94.

Nishikawa, Y., Fujisawa, T., Inoko, Y. & Moritoki, M. (2001). *Nucl. Instrum. Methods Phys. Res. A*, **467/468**, 1384–1387.
Patel, I. S. & Schmidt, P. W. (1971). *J. Appl. Cryst.* **4**, 50–55.
Paterson, M. S. (1982). *Bull. Minéral.* **105**, 20–29.
Poelman, D., DeGryse, O., DeRoo, Janssens O. & Clauws, P. (2004). *J. Appl. Phys.* **96**, 6164–6168.
Suzuki, C. K., Iwasaki, F. & Kohra, K. (1980). *Proceedings of the 34th Annual Symposium on Frequency Control*, pp. 14–24.
Suzuki, S. & Nakashima, S. (1999). *Phys. Chem. Miner.* **26**, 217–225.
Ullrich, H. J., Schlaubitz, M., Friedel, F., Spann, T., Bauch, J., Wroblewski, T., Garbe, S., Gaul, G., Knöchel, A., Lechtenberg, F., Rossmanith, E., Kumpat, G. & Ulrich, G. (1994). *Nucl. Instrum. Methods Phys. Res. A*, **349**, 269–273.
Vainshtein, B. K. (1996). *Modern Crystallography 1: Fundamentals of Crystals. Symmetry, and Methods of Structural Crystallography*. Berlin: Springer.